Petroleum Science 23 (2026) 7142–7154

Contents lists available at ScienceDirect

Petroleum Science

journal homepage: www.keaipublishing.com/en/journals/petroleum-science

Original Paper

Microseismic signal denoising via a dynamically guided two-stage framework

Yi-Fei Bao [a,*], Jian Gao [a,b,c], Zi-Xiang Yan [a,b], Jing-Hua Xiao [a]

[a] School of Physical Science and Technology, Beijing University of Posts and Telecommunications, Beijing, 100876, China
[b] National Key Laboratory of Plasma Physics, and China Academy of Engineering Physics, Mianyang, 621900, Sichuan, China
[c] State Key Laboratory of Information Photonics and Optical Communications, Beijing University of Posts and Telecommunications, Beijing, 100876, China

ARTICLE INFO

Article history:
Received 30 March 2026
Received in revised form
29 May 2026
Accepted 19 July 2026
Available online 23 July 2026

Edited by Jie Hao

Keywords:
Microseismic
Denoising
Dynamical system
Reservoir computing
Bidirectional long short-term memory network

ABSTRACT

Microseismic signal denoising is a crucial step in microseismic monitoring because it directly affects the reliability of subsequent processing and interpretation. To address the low amplitude feature of microseismic signals, the complexity and nonstationarity of background noise, and the limitations of existing data-driven and physics-guided methods, this study proposes RC-BiLSTM, a lightweight two-stage denoising framework based on a dynamical-system consistency prior. Rather than imposing an explicit physics-constrained residual, the proposed framework uses a soft dynamical prior to represent noisy microseismic records as the superposition of a temporally coherent dominant component and stochastic perturbations. In the first stage, reservoir computing (RC) performs coarse denoising by representing the dominant dynamical features of the waveform in a high-dimensional recurrent state. In the second stage, the RC estimate and the explicit residual are fed into a bidirectional long short-term memory network (BiLSTM), which learns a residual refinement to recover weak waveform details and suppress complex nonstationary noise. Numerical experiments on both synthetic and field data demonstrate that RC-BiLSTM achieves effective denoising performance under the tested conditions and exhibits improved stability under medium-parameter perturbations. Field-data tests further suggest its potential for improving microseismic waveform quality in practical monitoring scenarios.
© 2026 The Authors. Publishing services by Elsevier B.V. on behalf of KeAi Communications Co. Ltd. This is an open access article under the CC BY license (http://creativecommons.org/licenses/by/4.0/).

1. Introduction

Microseismic monitoring is an important technique for characterizing fracture propagation and evaluating reservoir stimulation during hydraulic fracturing, and the quality of the recorded data directly affects the reliability of subsequent data processing and interpretation (Anikiev et al., 2023; Warpinski, 2009; Zhang, 2021). However, microseismic signals are typically characterized by low amplitude, short duration, and low signal-to-noise ratio (SNR). In practical monitoring, they are highly susceptible to complex nonstationary background noise, which makes effective phase identification difficult (Li et al., 2022). Therefore, achieving high-precision microseismic denoising under weak signals and complex noise environments is a key challenge in microseismic monitoring (Han and Van der Baan, 2015).

Traditional seismic signal denoising methods can be broadly categorized into frequency-domain or time-frequency-domain filtering, subspace decomposition, and predictive modeling. For example, Schimmel and Gallart (2007) combined band-pass filtering with offset and slowness to improve the denoising performance. Mousavi and Langston (2016) integrated continuous wavelet transforms, hybrid block thresholding, and higher-order statistics to improve amplitude preservation. The iterative tensor robust principal component analysis (TRPCA) used singular value decomposition (SVD) as a low-rank recovery engine (Anvari et al., 2018). An improved fast-matching pursuit (FMP) algorithm was developed by incorporating variational mode decomposition (VMD) for high-resolution seismic data reconstruction (Wang et al., 2024). Although these methods have been effective in conventional seismic denoising, they generally rely on assumptions such as spectral separability, local stationarity, linear predictability, or low-rank structure (Lin et al., 2023). For microseismic data, however, such assumptions are often challenged by low SNR,

* Corresponding author.
E-mail address: byffly@bupt.edu.cn (Y.-F. Bao).
Peer review under the responsibility of China University of Petroleum (Beijing).

https://doi.org/10.1016/j.petsci.2026.07.039
1995-8226/© 2026 The Authors. Publishing services by Elsevier B.V. on behalf of KeAi Communications Co. Ltd. This is an open access article under the CC BY license (http://creativecommons.org/licenses/by/4.0/).

strong nonstationarity, and substantial overlap between the time-frequency signatures of signal and noise, making it difficult to simultaneously recover weak events and suppress complex noise (Zhu et al., 2019). Furthermore, the performance of many traditional methods is sensitive to parameter settings such as window length and threshold values, resulting in substantial empirical tuning and limited automation (Meng et al., 2022).

With the rapid development of deep learning in recent years, data-driven denoising methods have offered a new route for microseismic signal recovery in complex noisy environments. Convolutional neural networks (CNNs), owing to their ability to extract local waveform structures and multiscale features (LeCun et al., 2015), have been widely used for denoising tasks. Representative approaches include residual CNNs, DnCNN, and convolutional denoising networks that process multichannel records as two-dimensional images (Li et al., 2022; Duan et al., 2025; Sang et al., 2021; Zhang et al., 2020). Building on this line of work, U-Net further improves the preservation of effective phases through multiscale feature fusion (Chen et al., 2024). Because microseismic signals exhibit pronounced temporal characteristics, recurrent neural networks (RNNs) and their variants, such as LSTM, have also been introduced for denoising tasks to compensate for the limited long-range modeling capability of pure CNNs, thereby enhancing the representation of temporal relationships and long-term dependencies (Novoselov et al., 2022). In addition, emerging architectures such as Transformers and diffusion models have shown strong capability in global feature extraction and characterization of complex noise (Peng et al., 2023; Sun et al., 2025). However, the generalization performance of such methods often degrades when the true noise type, spectral characteristics, or propagation conditions deviate from those represented in the training data (Zhang et al., 2025). More importantly, most existing data-driven deep learning methods rely on statistical patterns embedded in the training data and therefore exhibit limited interpretability (Huang and Alkhalifah, 2024).

Motivated by the limited interpretability of purely data-driven deep learning methods, recent studies have begun to incorporate explicit physical constraints or geophysical-guided prior into deep learning models. Representative approaches can be broadly divided into two categories. One introduces the residuals of governing equations, such as the wave equation and the Helmholtz equation, into the loss function, giving rise to physics-informed neural network (PINN) methods (Brandolin et al., 2024; Rasht-Behesht et al., 2022; Shao et al., 2024; Yuan et al., 2025). Another strategy leverages geophysical attributes to construct guidance information or soft constraints, thereby improving the consistency between network outputs and physical laws. Xie et al. (2025) integrated velocity-dependent slope estimation into local plane-wave constraints and combined Fourier embeddings with periodic activation functions to suppress random and erratic noise. Zhao and Rao (2024) incorporated local seismic dip information into both the network architecture and the objective function to build a structure-preserving deep denoising convolutional neural network (SP-DnCNN), which efficiently suppresses broadband random noise and improves the preservation of complex structural features in seismic data. These methods endow the model with interpretability and ensure the reliability of the denoising results. However, they are often sensitive to the quality of prior models. When prior parameters are biased, the associated constraints or guidance information may become mismatched (Yao et al., 2020), thereby degrading the stability and accuracy of the network output. Moreover, physics-constrained methods relying on automatic differentiation usually require high training costs, making them difficult to deploy for large-scale data processing under limited computational resources (Mu et al., 2025).

To address the above issues, this study proposes a lightweight two-stage microseismic denoising framework, RC-BiLSTM, based on a dynamical-system consistency prior. Different from strictly physics-constrained methods that explicitly impose governing-equation residuals, the proposed framework adopts a softer form of dynamical guidance. From the perspective of stochastic dynamical-system reconstruction, the temporal evolution of microseismic signals is described by approximating noisy field data as the superposition of a dominant deterministic component and a stochastic perturbation component. Accordingly, the denoising task is formulated as the recovery of the dominant dynamical orbit, which provides the framework with a dynamical interpretation. At the model level, the first stage introduces RC to construct a high-dimensional recurrent state space induced by fixed random connections, whose recurrent nonlinear dynamics are used to capture the dominant dynamical characteristics of microseismic signals (Wang et al., 2022). By training only the linear readout layer, coarse denoising is achieved at low computational cost (Gauthier et al., 2021). In the second stage, the RC estimate and its explicit residual are jointly fed into a BiLSTM, which exploits its ability to capture long-range dependencies in temporal data to further refine residual errors and weak-phase details under complex nonstationary noise (Lee et al., 2024). Numerical experiments on both synthetic and field data are conducted to evaluate the denoising capability of the proposed framework. Moreover, perturbation experiments on medium parameters are designed to assess the sensitivity of RC-BiLSTM to prior models. Overall, the RC-BiLSTM framework offers a robust and efficient solution that effectively mitigates the impact of prior model inaccuracies, while providing a dynamical interpretation to the denoising process.

2. Methodology

2.1. Overall framework

This study proposes a two-stage microseismic denoising framework, RC-BiLSTM, as shown in Fig. 1. The first step is to generate paired training data. Using medium parameters available for the study area, the reflectivity method is employed to perform forward modeling of a noise-free synthetic microseismic signal $s(t)$. Noise samples are then extracted from field data and

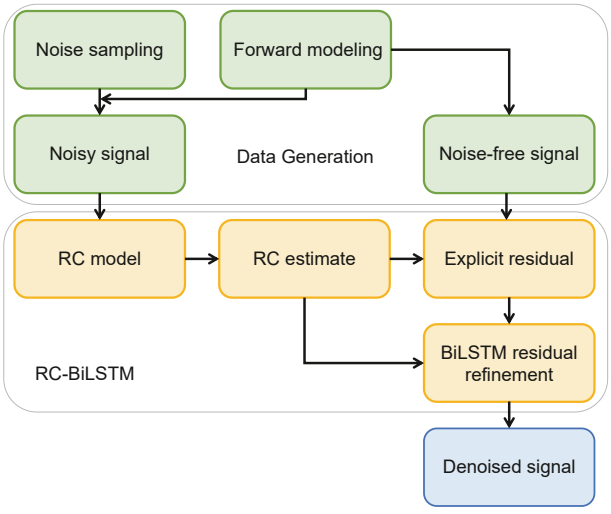


Fig. 1. Pipeline of the proposed RC-BiLSTM denoising framework.

combined with synthetic noise. After random scaling, a noise term $n(t)$ is obtained and superposed on $s(t)$ to construct the noisy data $x(t)$:

$$x(t) = s(t) + n(t), \tag{1}$$

The denoising framework adopts a two-stage strategy consisting of RC-based coarse denoising followed by BiLSTM-based residual refinement. In the first stage, RC is used to perform coarse denoising on $x(t)$ and to obtain the RC estimate $\widehat{s}_{RC}(t)$. By using a high-dimensional recurrent state space as a universal basis-function set and training only a linear readout layer, RC can characterize the dominant deterministic evolution structure of microseismic signals at low computational cost, which appears in the waveform domain as temporally coherent dominant waveform components. Accordingly, RC introduces a dynamical-system consistency prior in a soft form, guiding the first-stage output toward coherent signal evolution without imposing an explicit governing-equation constraint. In the second stage, the explicit residual between the RC estimate $\widehat{s}_{RC}(t)$ and the noisy data $x(t)$ is computed as $e(t)$:

$$e(t) = x(t) - \widehat{s}_{RC}(t). \tag{2}$$

The explicit residual $e(t)$ represents the discrepancy between the noisy input and the RC estimate. Because the RC stage performs only coarse denoising, its output may suppress a large part of the stochastic perturbation but may also leave residual nonstationary noise or attenuate weak waveform details. The residual channel therefore provides complementary information that is not fully contained in the RC estimate alone. The explicit residual $e(t)$ and the RC estimate $\widehat{s}_{RC}(t)$ are then jointly fed into the BiLSTM, allowing it to focus on learning the residual refinement mapping between the RC estimate and the noise-free signal, $\Delta(t)$, thereby improving the recovery of weak phases and the suppression of complex nonstationary noise. The final output is given by:

$$\widehat{s}(t) = \widehat{s}_{RC}(t) + \Delta(t). \tag{3}$$

In this framework, the two stages are trained sequentially. The RC is responsible for capturing the dominant deterministic evolution structure, while the BiLSTM refines the complex residual errors that RC cannot fully capture.

2.2. Dynamical-systems perspective and interpretation

Inspired by the perspective of stochastic dynamical-system reconstruction, this study conceptualizes microseismic field data as a stochastic dynamical system composed of deterministic dynamics and stochastic perturbations, thereby interpreting denoising as the recovery of a deterministic orbit. Let the microseismic signal be $y(t)$, which can be approximately described by the following stochastic dynamical system:

$$\dot{y} = f(y(t)) + \eta(t), \tag{4}$$

where $f(\cdot)$ denotes the unknown deterministic dynamical term jointly governed by source radiation, wavefield propagation, and site response, and $\eta(t)$ denotes the stochastic perturbation term. The denoising objective is formulated as the recovery of the noise-free signal $y_0(t)$ under complex noise environments, which satisfies:

$$\dot{y_0} = f(y_0(t)), y_0(0) = y(0). \tag{5}$$

To avoid the instability caused by differentiating noisy data, Eq. (4) is written in its integral form:

$$y(t) = y(0) + \int_0^t f(y(\tau))\mathrm{d}\tau + \int_0^t \eta(\tau)\mathrm{d}\tau. \tag{6}$$

Within a local time window, a second-order approximation of Eq. (6) is written as:

$$y(t)^{(2)} = y(0) + \int_0^t f\left(y^{(1)}(\tau)\right)\mathrm{d}\tau + \int_0^t \eta(\tau)\mathrm{d}\tau, \tag{7}$$

where $y^{(1)}(\tau)$ is the first-order approximation of Eq. (6). Around the arrivals of the P and S waves in microseismic records, waveforms typically exhibit pronounced transient changes and high local curvature. A second-order Taylor approximation can better capture these structural characteristics within a local window. Accordingly, a second-order Taylor expansion of the deterministic term $f\left(y^{(1)}(\tau)\right)$ is taken and then ensemble-averaged, yielding the following approximation to the deterministic component of the average orbit:

$$\langle y^{(2)}(t)\rangle = y(0) + f(y(0))t + \frac{1}{2}f(y(0))f'(y(0))t^2 + \frac{1}{2}Df''(y(0))t^2, \tag{8}$$

where D denotes the strength of the stochastic perturbation. The Taylor expansion of the noise-free signal in Eq. (5) can be written as:

$$y_0(t) = y_0(0) + f(y_0(0))t + \frac{1}{2}f(y_0(0))f'(y_0(0))t^2 + O\left(t^3\right). \tag{9}$$

Comparing Eq. (8) and Eq. (9) suggests that the deterministic component of the average orbit $\langle x^{(2)}(t)\rangle$ and the noise-free signal $s_0(t)$ are consistent at the level of first-order local evolution, whereas their difference appears only in higher-order terms. Because the stochastic perturbation lacks sustained temporal coherence, its influence is strongly weakened under local averaging or high-dimensional recurrent state mapping. Therefore, it provides a dynamically consistent surrogate, indicating that microseismic denoising can be treated as the recovery of the dominant deterministic evolution structure embedded in the field data under complex noise environments. Accordingly, the average orbit can be regarded as a dynamically consistent approximation to the dominant evolution structure of the noise-free microseismic signal.

Existing average orbit construction methods usually divide the full orbit into many very short segments, write the same local expression for each segment, and require that this expression hold over all time windows. A joint least-squares fit is then performed over all windows and sampling points to compute the average orbit. However, this approach depends on manually designed basis functions and is therefore relatively cumbersome. In this study, the high-dimensional recurrent state space induced by fixed random connections in reservoir computing is used as a universal set of basis functions to approximate the local evolution. In this way, a dynamical-system consistency prior is imposed on the deterministic evolution law of the signal without explicitly solving the governing equations, while simultaneously enabling first-stage coarse denoising.

2.3. RC architecture

For subsequent numerical implementation, the continuous-time signal is discretized from this point onward with sampling interval Δt and written as follows:

$$x[k]=x(k\Delta t), s[k]=s(k\Delta t), n[k]=n(k\Delta t), e[k]=e(k\Delta t),$$

$$\widehat{s}[k]=\widehat{s}(k\Delta t), \widehat{s}_{RC}[k]=\widehat{s}_{RC}(k\Delta t), \Delta[k]=\Delta(k\Delta t), k=1,2,...,T. \tag{10}$$

RC originates from recurrent-network paradigms such as the Echo State Network (ESN) and Liquid State Machine (LSM), and its standard architecture comprises an input layer, a reservoir, and a linear readout layer (Fig. 2). The reservoir contains D_r nodes, and the reservoir state vector is $\boldsymbol{r}[k] \in R^{D_r}$. The input layer couples the field data to the reservoir through the random input-weight matrix $\boldsymbol{W}_{\text{in}} \in R^{D_r \times D_{\text{in}}}$. Internal reservoir connections are described by the adjacency matrix $\boldsymbol{A} \in R^{D_r \times D_r}$, which is initialized as a sparse random Erdős–Rényi matrix. Its scale is treated as a task-dependent hyperparameter chosen to balance fading memory, nonlinear richness, and stable state evolution in the present denoising task. For the single-channel microseismic denoising task, both the input and the output are one-dimensional sequences, so $D_{\text{in}} = D_{\text{out}} = 1$.

The leaky-integrator RC state update and linear readout can be written as:

$$\boldsymbol{r}[k] = (1-\alpha)\boldsymbol{r}[k-1] + \alpha \tanh(\boldsymbol{A}\boldsymbol{r}[k-1] + \boldsymbol{W}_{\text{in}}x[k]), \tag{11a}$$

$$\widehat{s}_{RC}[k] = \boldsymbol{W}_{\text{out}}\boldsymbol{r}[k], \tag{11b}$$

where α is the leakage rate and $\boldsymbol{W}_{\text{out}} \in R^{D_{\text{out}} \times D_r}$ is the linear readout weight matrix. The input and reservoir weights in RC are fixed random matrices and are not trained; only the linear readout layer is solved, so the training and inference costs are substantially lower than those of end-to-end deep networks.

Given a training sample pair (x,s), the noisy input sequence $x[k]$ is first used to drive the reservoir to obtain the state sequence $\{\boldsymbol{r}[k])\}_{k=1}^{T}$. After discarding the initial washout segment τ, the state matrix and target matrix are constructed as follows:

$$\boldsymbol{H} = [\boldsymbol{r}[\tau+1], \boldsymbol{r}[\tau+2], \ldots, \boldsymbol{r}[T]] \in R^{D_r \times N}, \tag{12a}$$

$$\boldsymbol{S} = [\boldsymbol{s}[\tau+1], \boldsymbol{s}[\tau+2], \ldots, \boldsymbol{s}[T]] \in R^{D_{\text{out}} \times N}, \tag{12b}$$

where $N = T - \tau$. The linear readout layer is obtained in closed form by ridge regression:

$$\boldsymbol{W}_{\text{out}} = \boldsymbol{S}\boldsymbol{H}^{\top}\left(\boldsymbol{H}\boldsymbol{H}^{\top} + \lambda_{\text{ridge}}\boldsymbol{I}\right)^{-1}. \tag{13}$$

where $\boldsymbol{I}$ is the identity matrix and λ_{ridge} is the ridge regression parameter. The resulting $\widehat{s}_{RC}[k]$ is taken as the RC estimate.

The reservoir states are initialized to zero at the beginning of each input sequence. The first τ sampling points were discarded as the washout period to reduce the influence of the initial transient response. In this study, a reasonable candidate range of τ was first determined based on empirical considerations, the input sequence length, and the fading-memory behavior of the reservoir. The final value was then selected by grid search on the validation set, and τ was set to 100 sampling points yielded the lowest validation error. The main RC hyperparameters are as follows: the reservoir size is 50; the connection probability of the reservoir network is 0.332; the spectral radius of the adjacency matrix $\boldsymbol{A}$ is 0.935; the ridge-regression parameter is 1.571×10^{-4}; and the leakage rate, α, is 0.6279.

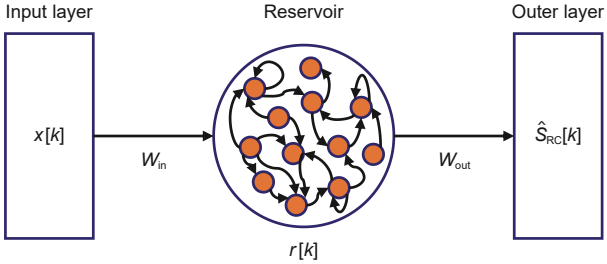


Fig. 2. Architecture of the reservoir computing module.

It should be noted that the dynamical interpretation of the RC stage is based on the stochastic dynamical-system approximation introduced above, and RC is therefore more effective at recovering the dominant deterministic evolution structure. Under this approximation, the stochastic perturbation term is treated as a short-correlation residual term in the local analysis. Its influence can be attenuated, but not completely eliminated, by local averaging and recurrent-state lifting. Consequently, RC alone is limited in dealing with fine waveform details, strongly nonstationary noise, and high-order residuals, as shown in Fig. 3. For this reason, a BiLSTM is introduced as the second-stage residual refinement module.

2.4. BiLSTM architecture

A BiLSTM architecture, comprising forward and backward LSTMs, is employed to capture bidirectional temporal dependencies. Unlike standard RNNs, the gated memory units in LSTM effectively mitigate gradient vanishing during long-sequence training, enabling the network to better capture the long-range correlations of microseismic signals in structures such as arrival times and seismic phases. Compared with a unidirectional LSTM, BiLSTM exploits symmetric contextual information both before and after an event, making it more effective at distinguishing temporally continuous and coherent waveforms from more random nonstationary noise under low SNR environments, thereby improving the fidelity of denoising. Furthermore, compared to attention-based architectures like Transformers, the BiLSTM offers a significantly lower computational cost. Combined with the RC estimate from the first stage, the BiLSTM only needs to learn a residual mapping of relatively low amplitude and complexity. This not only reduces the risk of overfitting, but also preserves the dynamical consistency and interpretability of the RC estimate to a large extent. On this basis, the RC estimate obtained from the linear readout layer is denoted by $\widehat{s}_{RC}[k]$, and the explicit residual $e[k]$ is constructed. The input feature at each sampling instant is then defined as:

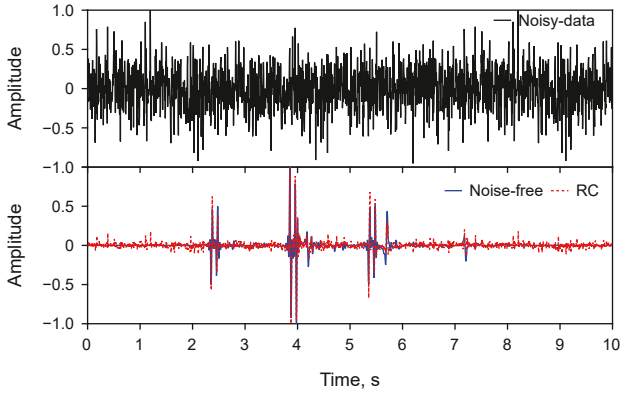


Fig. 3. Comparison of the RC-denoised signal with the noise-free signal. Black solid line denotes the input noisy signal. The blue solid line and the red dashed line represent the noise-free reference and the denoised signal, respectively.

$$\boldsymbol{u}[k] = \{\widehat{s}_{RC}[k], e[k]\} \in \boldsymbol{R}^2. \tag{14}$$

This generates the feature sequence $\boldsymbol{U} = \{\boldsymbol{u}[1], \boldsymbol{u}[2], ..., \boldsymbol{u}[t]\}$, which is then fed into the BiLSTM. Because $\boldsymbol{u}[k]$ contains both the dynamical backbone provided by RC and its associated discrepancy with the noisy data, the BiLSTM does not need to reconstruct the entire signal mapping. Instead, it can focus on learning a residual correction for the components that are not fully recovered by RC, thereby improving the overall denoising accuracy while preserving the dynamical consistency inherent in the RC estimate.

The composite mapping consisting of the BiLSTM and its integrated linear readout layer is represented by $\boldsymbol{\Phi}_{\mathrm{BiLSTM}}(\cdot, \theta)$, where θ denotes all trainable parameters. The residual refinement sequence can then be expressed as:

$$\boldsymbol{\Delta}[1:T] = \boldsymbol{\Phi}_{\mathrm{BiLSTM}}(\boldsymbol{U}, \theta). \tag{15}$$

The final denoised output is given by:

$$\widehat{s}[k] = \widehat{s}_{RC}[k] + \Delta[k]. \tag{16}$$

Given that the primary objective of the second stage is to refine the residuals unmodeled by the RC, this study adopts a loss objective that integrates residual supervision with a multi-resolution STFT spectral constraint. The ground-truth residual is defined as:

$$\Delta^*[k] = s[k] - \widehat{s}_{RC}[k]. \tag{17}$$

The corresponding residual loss is written as:

$$L_{\mathrm{res}} = \frac{1}{T}\sum_{k=1}^{T} \|\Delta[k] - \Delta^*[k]\|_1. \tag{18}$$

To further enforce spectral consistency and preserve intricate spectro-temporal features in the denoised result, a multi-resolution STFT spectral loss is adopted:

$$L_{\mathrm{spe}} = \frac{1}{M}\sum_{m=1}^{M} \Big[\big\| |\mathrm{STFT}_m(\widehat{s})| - |\mathrm{STFT}_m(s)| \big\|_1 + \big\| \log(|\mathrm{STFT}_m(\widehat{s})| + \varepsilon) - \log(|\mathrm{STFT}_m(s)| + \varepsilon) \big\|_1 \Big], \tag{19}$$

where M denotes the number of STFT resolutions, ε is a constant introduced to avoid numerical instability in the logarithm and is set to 10^{-6}. In the multi-resolution STFT loss, three resolutions were used. The window lengths were set to 128, 256, and 512 samples, the corresponding hop sizes were 32, 64, and 128 samples, and the FFT sizes were 128, 256, and 512, respectively. A Hann window was used for all STFT calculations. The total loss function is defined as:

$$L = L_{\mathrm{res}} + \sigma_{\mathrm{spe}} L_{\mathrm{spe}}, \tag{20}$$

where σ_{spe} is the weight of the spectral loss and is set to 0.2.

The main BiLSTM hyperparameters are as follows: the network has 2 layers, the hidden-state dimension is 64, the dropout probability is 0.2, and the readout structure is a linear layer of size 2H→1. The optimizer is Adam, the initial learning rate is 0.001, the batch size is 256, and the maximum number of training epochs is 20.

The hyperparameters of the RC and BiLSTM modules were selected using Bayesian optimization on the validation set. For the RC stage, the validation mean square error between the RC estimate and the clean reference signal was used as the objective. For the BiLSTM stage, the total validation loss defined in Eq. (20) was used as the objective. The Bayesian optimization process searched the predefined parameter ranges listed in Table 1, and the final hyperparameter combination with the lowest validation loss was used for testing.

Table 1
Search ranges and selected values of the main hyperparameters in Bayesian optimization.

Module	Hyperparameter	Search range	Selected value
RC	Reservoir size	20–200	50
	Connection probability	0.05–0.50	0.332
	Spectral radius	0.5–1.10	0.935
	Leakage rate	0.1–1.00	0.6279
	Ridge-regression parameter	10^{-6}-10^{-2}	1.571×10^{-4}
BiLSTM	Number of BiLSTM layers	1-5	2
	Hidden-state dimension	32-256	64
	Dropout probability	0-0.5	0.2
	Learning rate	0.0001-0.01	0.001
	Batch size	64-512	256

2.5. Data generation

From 2020 to 2022, 50 MEMS stations in the Zigong-Neijiang area of Sichuan Province recorded nearly 10,000 microseismic field data, most of which had magnitudes below 3 and relatively low SNR. The training and evaluation data used in this study were constructed on the basis of the microseismic field data and geological information from this study area.

For training data, strictly noise-free labels are difficult to obtain. Therefore, this study adopted a paired-data strategy in which noise-free signals were generated through forward modeling and noisy inputs were constructed by superimposing noise segments extracted from field data onto synthetic noise-free signals. Specifically, the layered model given by Lai et al. (2023) (Table 2) was used in reflectivity-based forward modeling. To match the actual distribution more closely, sources were clustered, and 200 receivers were deployed at 0.1 km spacing within an epicentral distance of 20 km. Consistent with local geology, three sets of thrust-fault focal mechanism parameters with distinct orientations were considered. Table 3 lists the focal depths and focal-mechanism parameters of one set. In total, 3600 synthetic data were generated and amplitude-normalized, forming the noise-free dataset. The dataset was then randomly divided into training, validation, and test subsets with a ratio of 70%/20%/10%, where the validation set was used for model selection and hyperparameter tuning, and the test set was reserved exclusively for final performance evaluation.

To construct noise samples, 200 microseismic field data were randomly selected, and time windows far from any identifiable seismic phases were extracted as noise samples. To ensure spatial representativeness, the selected field data covered different station azimuths and epicentral distances as much as possible. To reduce leakage of noise samples, the noise records were also

Table 2
1D layered medium parameters used for forward modeling.

Depth, km	P-wave velocity, km/s	S-wave velocity, km/s	Density, g/cm^3
0	4.63	2.72	2.6
2	4.87	2.86	2.66
4	5.19	3.05	2.9
6	5.55	3.26	2.9
8	5.73	3.37	3.06

Table 3
Focal depths and focal-mechanism parameters for one of the three source-parameter sets used for forward modeling.

Focal depth, km	Strike, °	Dip, °	Rake, °
1.5	45	30	90
2.5	120	40	85
3.5	210	25	95
4.5	330	35	105
5.5	80	45	75
6.5	270	20	115

divided into exclusive training, validation, and test subsets using the same proportions as the noise-free dataset. Within each subset, each selected noise record was amplitude-normalized and adjusted to 0.5 times the maximum amplitude of the corresponding noise-free signal. These records were then randomly scaled by a factor in the range of [0.5, 2.0] to generate 16 different noise samples representing real noise at different intensities. A total of 3200 real-noise samples were generated from the 200 field data. In addition, to enrich the diversity of noise samples and further improve model generalization, 400 synthetic noise samples were introduced, including Gaussian noise, band-limited noise, and power-line interference, and were likewise divided into three subsets. The Gaussian noise was used to simulate random measurement error and instrumental background noise commonly present in microseismic field data. And the band-limited noise was introduced to approximate interference within specific frequency bands. The power-line interference was applied to characterize the typical periodic narrowband noise induced by electrical equipment. Finally, the generated noise signals were superposed on the simulated noise-free signals, producing a total of 3600 synthetic noisy samples.

Finally, to evaluate the distribution mismatch caused by uncertainty in medium parameters, an additional medium-perturbed test dataset was constructed on the basis of the reference layered model (Table 2). Keeping the noise sampling unchanged, independent random relative perturbations were applied to the layered medium parameters used in forward modeling. The perturbation level was set to $\delta \in \{10\%, 20\%, 30\%, 40\%\}$. The corresponding noise-free datasets were then generated, with 90 samples for each perturbation level, giving a total of 360 samples. The same noise-superposition strategy as that used for the reference test set was then applied to generate the corresponding perturbed test dataset.

All neural-network models were implemented in Python 3.9 using PyTorch 2.0. The experiments were conducted on a workstation equipped with GPU-RTX4090 (24 GB), CPU-I9 14900K.

3. Numerical experiments

To systematically evaluate the denoising performance of RC-BiLSTM and its adaptability to uncertainty in medium parameters, experiments were conducted on both synthetic and field data. The synthetic data experiments included denoising comparisons, robustness analysis under uncertain medium parameters, and ablation studies. The field data experiments involved tests on datasets from the Zigong–Neijiang area and the Tulsa area.

3.1. Synthetic data

3.1.1. Denoising comparison

To evaluate the denoising performance of RC-BiLSTM, the comparison covered both conventional denoising methods and deep learning models. These denoising methods included wavelet-transform, a purely data-driven CNN-BiLSTM model, and a geophysics-guided SP-DnCNN model. Among them, CNN-BiLSTM and SP-DnCNN are representative deep learning denoising models reported in recent studies and have shown strong denoising capability in related applications. The hyperparameter combinations of all comparison models were selected by grid search on the validation set, and the test results corresponding to the best validation performance are reported. For the CNN-BiLSTM model, the selected architecture consisted of five one-dimensional convolutional layers, a convolutional kernel size of 3, ReLU activation, followed by two BiLSTM layers with a hidden-state dimension of 128 and a dropout probability of 0.1. For the SP-DnCNN model, the selected architecture consisted of 8 one-dimensional convolutional layers with a kernel size of 3, 64 filters in the hidden layers, same padding, batch normalization, ReLU activation, and residual learning. Both deep-learning comparison models were trained using the Adam optimizer with an initial learning rate of 0.001 and 20 training epochs. The same training, validation, and test subsets, as well as the same waveform normalization and preprocessing procedures, were used for all deep-learning models to ensure a fair comparison.

To evaluate the denoising performance of different methods, the *SNR* and the correlation coefficient (*CC*) were adopted as evaluation metrics. *SNR* measures the improvement in effective signal energy relative to noise after denoising, whereas *CC* quantifies the similarity between the denoised result and the noise-free waveform. Their expressions are as follows:

$$SNR = 10 \log \frac{\|s\|_2^2}{\|\widehat{s} - s\|_2^2}, \tag{21a}$$

$$CC = \frac{\mathrm{cov}(s, \widehat{s})}{(\sigma(s) * \sigma(\widehat{s}))}, \tag{21b}$$

where $\mathrm{cov}(\cdot,\cdot)$ and $\sigma(\cdot)$ denote the covariance and standard deviation, respectively. Large values of *SNR* and *CC* indicate better denoising performance. In addition, we compared the maximum amplitude change rate (*MACR*) and the polarity change rate (*PCR*) of the denoised signals. These metrics provide a direct assessment of waveform fidelity, indicating whether the denoising process alters key signal features such as peak amplitude and the sign of the main waveform peak, which are critical for subsequent tasks like phase picking, event localization, and focal mechanism analysis.

Figs. 4 and 5 show two representative examples with different noisy signal quality. Figs. 4(a) and 5(a) correspond to a mildly noisy signal, whereas Figs. 4(b) and 5(b) correspond to a heavily contaminated case. In the time domain (Fig. 4), the wavelet method suppressed part of the noise, but it also attenuated weak phases and introduced a certain degree of waveform distortion. By contrast, CNN-BiLSTM, SP-DnCNN, and RC-BiLSTM all reconstructed the overall waveform structure more effectively (Fig. 4(a)). However, as the signal quality degraded (Fig. 4(b)), the denoising outcomes of CNN-BiLSTM and SP-DnCNN became suboptimal. They still recovered the major event, but both retained visible residual noise or local distortion. Conversely, the proposed RC-BiLSTM maintained high efficacy, delivering a more accurate denoising result.

Fig. 5 further compares the corresponding frequency-domain results. The wavelet method reduced part of the high-frequency noise, but it still introduced pronounced spectral artifacts and distorted the effective-band boundaries. CNN-BiLSTM and SP-DnCNN preserved the spectral shape better than the wavelet method, although spectral leakage and energy shifts remained

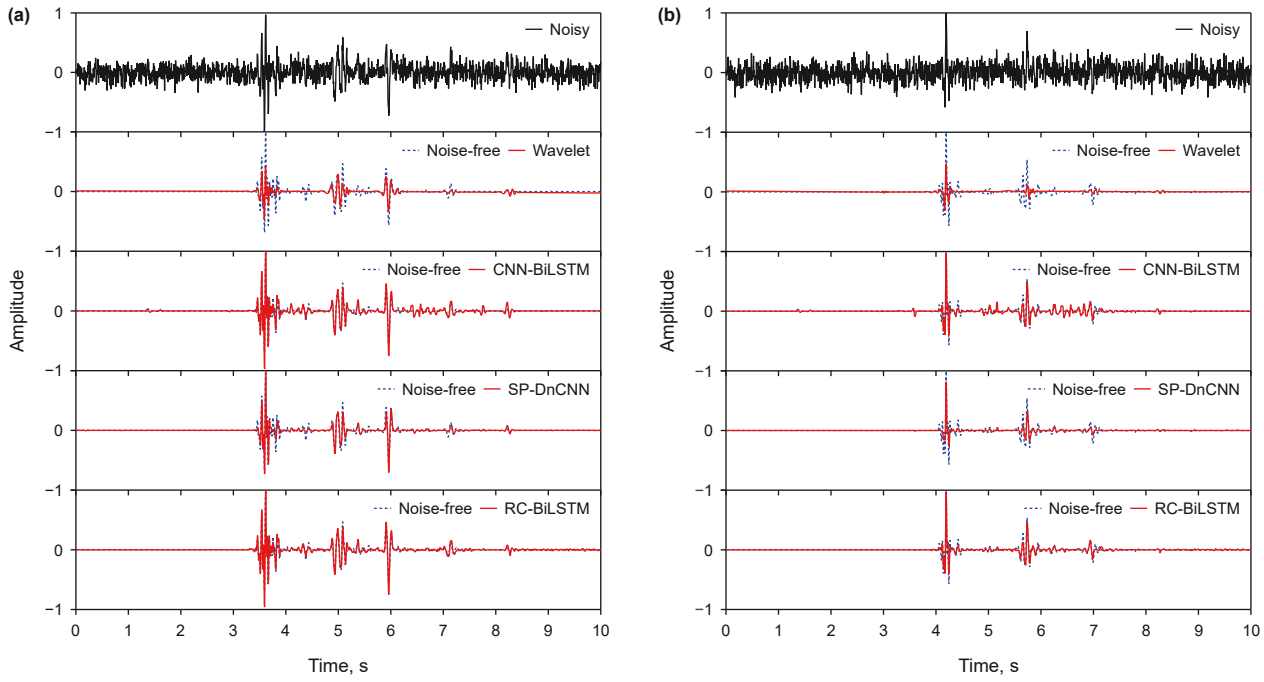


Fig. 4. Time-domain comparison of denoising results. The black solid line denotes the noisy input, the blue dashed line denotes the noise-free reference, and the red solid line denotes the denoised output.

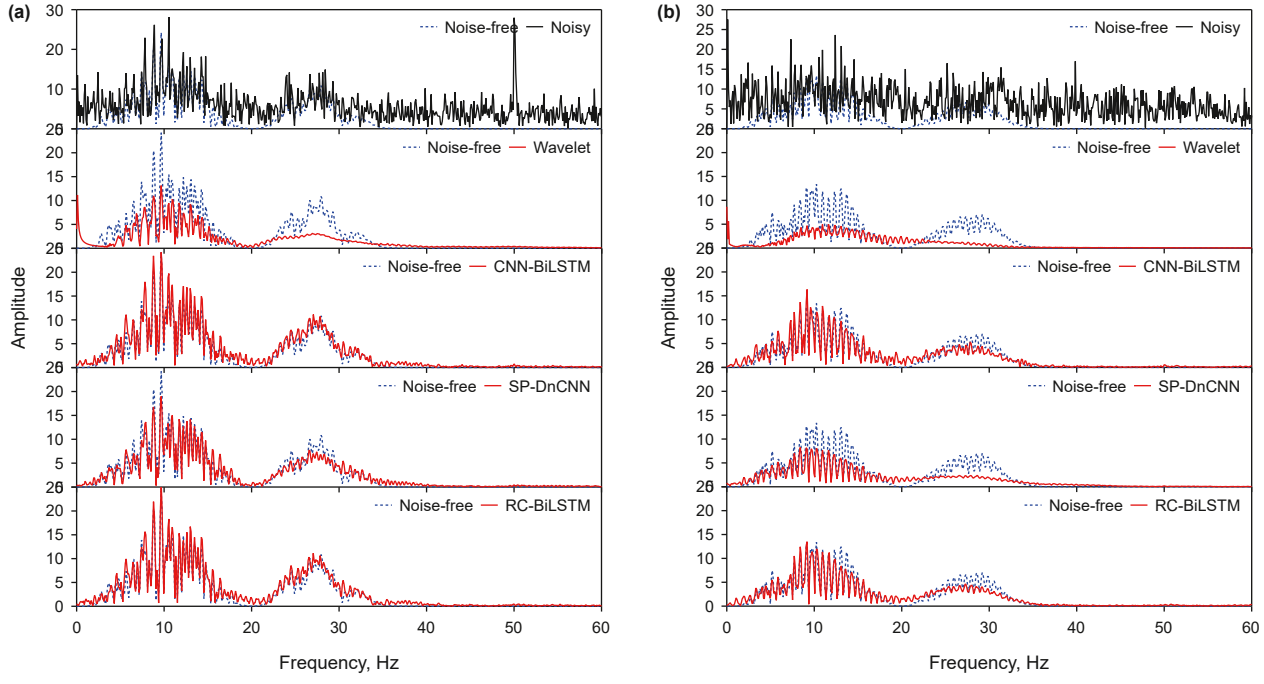


Fig. 5. Comparison of the frequency-domain denoising results of the different methods. The black solid line denotes the spectrum of the noisy signal, the blue dashed line denotes the spectrum of noise-free signal and the red solid line denotes the spectrum of the denoised signal.

visible, especially for the heavily noisy case in Fig. 5(b). By contrast, the spectrum produced by RC-BiLSTM was consistently closest to that of the noise-free signal for both examples. It suppressed out-of-band noise more effectively while preserving the main frequency band and local spectral peaks more faithfully.

The quantitative results in Table 4 are consistent with the visual observations. For the mildly noisy signal, RC-BiLSTM achieved the best *SNR* and *CC*, reaching 11.95 dB and 0.96, respectively, slightly outperforming CNN-BiLSTM (11.38 dB and 0.95) and SP-DnCNN (10.87 dB and 0.95). For the heavily noisy signal, its advantage became more markedly: RC-BiLSTM attained 9.65 dB and 0.94, compared with 7.36 dB and 0.91 for CNN-BiLSTM, and 6.88 dB and 0.89 for SP-DnCNN. Although the wavelet method improved the *SNR* relative to the raw input, it remained inferior to the deep learning models. Furthermore, Table 4 also compares the overall performance of the four

Table 4
Quantitative time-domain comparison of the different methods.

Metrics	Mildly noisy signal				
	Original data	Wavelet	CNN-BiLSTM	SP-DnCNN	RC-BiLSTM
SNR, dB	−1.74	4.51	11.38	10.87	11.95
CC	0.63	0.85	0.95	0.95	0.96
MACR	/	0.537	0.022	0.018	0.006
Metrics	Heavily noisy signal				
	Original data	Wavelet	CNN-BiLSTM	SP-DnCNN	RC-BiLSTM
SNR, dB	−8.45	3.27	7.36	6.88	9.65
CC	0.34	0.79	0.91	0.89	0.94
MACR	/	0.411	0.035	0.176	0.043
Metrics	All 360 signals in test subset				
	Original data	Wavelet	CNN-BiLSTM	SP-DnCNN	RC-BiLSTM
$\overline{SNR}$, dB	−3.36	3.62	9.13	8.87	11.56
$\overline{CC}$	0.56	0.83	0.93	0.93	0.95
$\overline{MACR}$	/	26.7%	8.4%	9.1%	5.9%
$\overline{PCR}$	/	6.7%	1.9%	2.2%	1.4%

methods across the entire test subset. The statistical trend aligns with the representative examples. The wavelet method improved the average SNR ($\overline{SNR}$) by approximately 7 dB over the raw inputs and improved the average CC ($\overline{CC}$) by 0.3. Both CNN-BiLSTM and SP-DnCNN achieved improvements of around 12 dB ($\overline{CC}$ improvement: ~0.4). The proposed RC-BiLSTM method delivered the highest $\overline{SNR}$ improvement of approximately 15 dB ($\overline{CC}$ improvement: ~0.4). In addition, we compared the average MACR ($\overline{MACR}$) and the average PCR ($\overline{PCR}$) across the test set, which further demonstrate that RC-BiLSTM preserves key waveform features more effectively than the comparison methods. These results indicate that the dynamical-system consistency prior introduced by the RC helps stabilize the recovery of the dominant deterministic evolution structure, while the subsequent BiLSTM residual refinement further improves denoising under complex nonstationary noise environments.

In addition, the total training times of different deep models were measured under the same hardware environment and unified training settings. The results show that CNN-BiLSTM required about 10 min for training, SP-DnCNN about 25 min, whereas RC-BiLSTM required less than 5 min. This indicates that RC-BiLSTM substantially reduces the training cost while maintaining denoising accuracy.

To further examine whether the trained framework introduces artificial events or unnecessarily modifies already clean seismic signals, two special-input tests were conducted. First, pure-noise records without effective microseismic signals were used as input to the trained RC-BiLSTM model. Since the expected signal component is zero in this case, an ideal denoising model should suppress the output and avoid generating event-like waveforms. Second, noise-free synthetic microseismic signals were directly used as input. In this case, an ideal denoising model should preserve the input waveform with minimal changes.

The results are shown in Fig. 6 and Table 5. For the pure-noise input, the RC-BiLSTM output was strongly suppressed and did not exhibit obvious phase-like waveform structures. The output energy ratio (OER) was defined as the ratio between the output energy and the input-noise energy, was 3.4%. It can be computed as:

$$OER = \frac{\|s\|_2^2}{\|n\|_2^2}, \tag{22}$$

where n denotes the pure-noise input and s denotes the model output. For the noise-free signal input, the output remained highly consistent with the clean input, with a *CC* of 0.99 and an Root mean square (RMS) error of 0.0067. These results indicate that the proposed framework has a low tendency to generate artificial events from pure-noise inputs and does not substantially distort already clean seismic signals under the tested conditions.

3.1.2. Robustness to medium parameters perturbation

To assess sensitivity to prior model inaccuracies, this study conducted robustness tests using perturbed medium parameters. Here, robustness is characterized as the stability of denoising performance against distribution shifts induced by forward-model deviations. CNN-BiLSTM, SP-DnCNN, and RC-BiLSTM were applied to the perturbed test dataset. While none of the models explicitly require medium parameters as input during inference, their performance is intrinsically tied to the prior model used for training data generation.

Fig. 7 shows the $\overline{SNR}$ of the different methods with different medium perturbation levels δ. Overall, the denoising performance of all methods decreased as the perturbation level increased, confirming that deviations in the forward model induce distribution shifts between training and test data. However, the sensitivity to these inaccuracies varied significantly among the models. The purely data-driven CNN-BiLSTM was most vulnerable, with its $\overline{SNR}$ dropping from 10.2 dB to 5.2 dB, reflecting its heavy reliance on the specific statistical patterns of the training distribution. Although the geophysics-guided SP-DnCNN slowed the performance decline (9.8 dB to 6.9 dB), it nevertheless exhibited a distinct sensitivity to prior model inaccuracies. In contrast, RC-BiLSTM demonstrated superior stability, with only a marginal decrease from 10.5 dB to 9.1 dB. These results indicate that even though the paired training labels are generated using the prior model, the RC-BiLSTM shows reduced sensitivity to medium-parameter mismatch.

3.1.3. Ablation study

To further verify the necessity of each component in RC-BiLSTM, an ablation study was conducted by constructing two degraded models and comparing them with the full model: an RC-only model and a BiLSTM-only model. A 40% perturbation level was selected as a representative case of severe model discrepancy for module-level analysis.

As shown in Table 6, the full model and its two ablated variants exhibit distinct behaviors under the reference medium and the strong mismatch conditions. On the reference test set, RC-BiLSTM achieved the highest *SNR*, reaching 10.7 dB, followed by BiLSTM-only (10.3 dB), whereas RC-only performed worse (7.4 dB). Under the 40% medium perturbation, however, the *SNR* of BiLSTM-only dropped to 5.6 dB, showing the largest degradation; RC-only decreased only slightly to 7.2 dB, indicating the smallest performance change; and RC-BiLSTM remained at 9.1 dB, achieving the best performance. These results indicate that, when used alone, the RC front end is less accurate than BiLSTM-only under the reference medium condition, but provides much better stability when the medium parameters are strongly perturbed. In contrast, although BiLSTM-only exhibits better denoising accuracy under the reference condition, it is more sensitive to medium mismatch. The full RC-BiLSTM model maintains denoising performance comparable to that of BiLSTM-only under the reference condition and performs

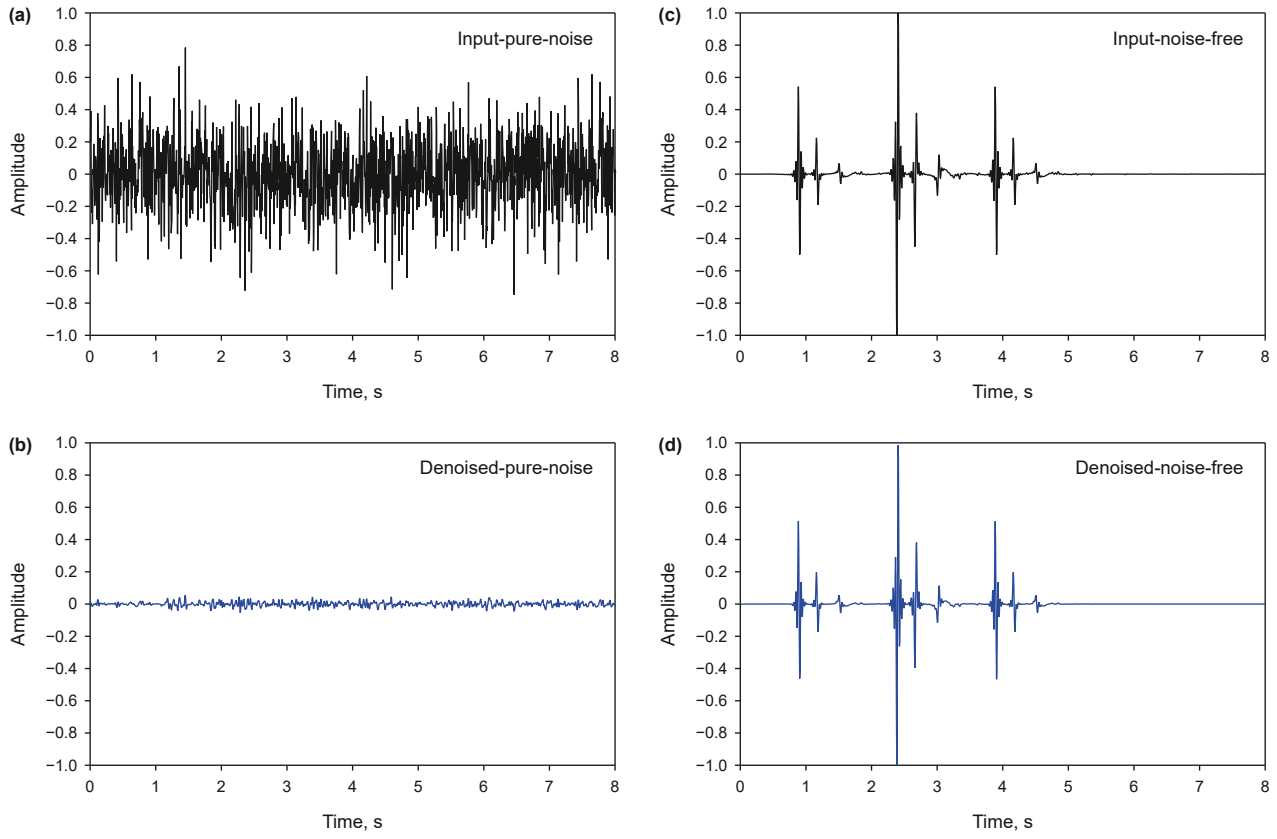


Fig. 6. Special-input tests of the trained RC-BiLSTM model. **(a)** Pure-noise input. **(b)** Output corresponding to the pure-noise input. **(c)** Clean seismic signal input. **(d)** Output corresponding to the clean-signal input.

Table 5
Special-input test results of the trained RC-BiLSTM model.

Input type	Evaluation metric	Value	Interpretation
Pure noise	*OER*	3.4%	The output energy is strongly suppressed, indicating no obvious artificial event generation.
Noise-free signal	*CC*	0.99	The output remains highly correlated with the input.
Noise-free signal	*RMS* error	0.0067	The waveform distortion is small.

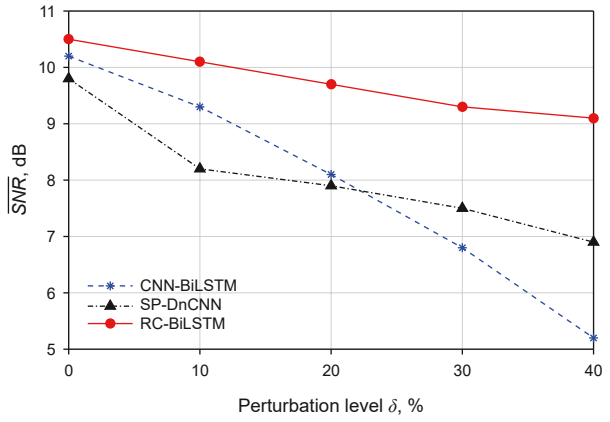


Fig. 7. Comparison of denoising performance across various perturbation levels δ. The blue dashed curve denotes the $\overline{SNR}$ of CNN-BiLSTM; the black dashed curve denotes the $\overline{SNR}$ of SP-DnCNN and the red solid curve denotes the $\overline{SNR}$ of RC-BiLSTM.

Table 6
Quantitative comparison of ablated models under the reference medium and a 40% medium perturbation.

Model	*SNR*, dB		
	BiLSTM-only	RC-only	RC-BiLSTM
Reference medium	10.3	7.4	10.7
40% medium perturbation	5.6	7.2	9.1

best under the 40% perturbation, which supports the design rationale of the proposed framework.

3.2. Field data

3.2.1. Zigong-Neijiang area

To assess the applicability of the proposed RC-BiLSTM in real scenarios, it was applied to microseismic field data recorded in the Zigong-Neijiang area from 2020 to 2022. Because strictly noise-free reference signals are unavailable for field data, a windowed *SNR*, was used as the quantitative evaluation metric:

$$SNR = 10\log 10\left(\frac{P_s}{P_n}\right). \tag{23}$$

where P_s and P_n denote the signal and noise powers within their respective time windows, defined as:

$$P_s = \frac{1}{T_s}\sum_{t\in T_s}\hat{s}^2(t), P_n = \frac{1}{T_n}\sum_{t\in T_n}\hat{s}^2(t), \tag{24}$$

Fig. 8 shows representative denoising results for field data from the Zigong-Neijiang area. The effective seismic phases in the

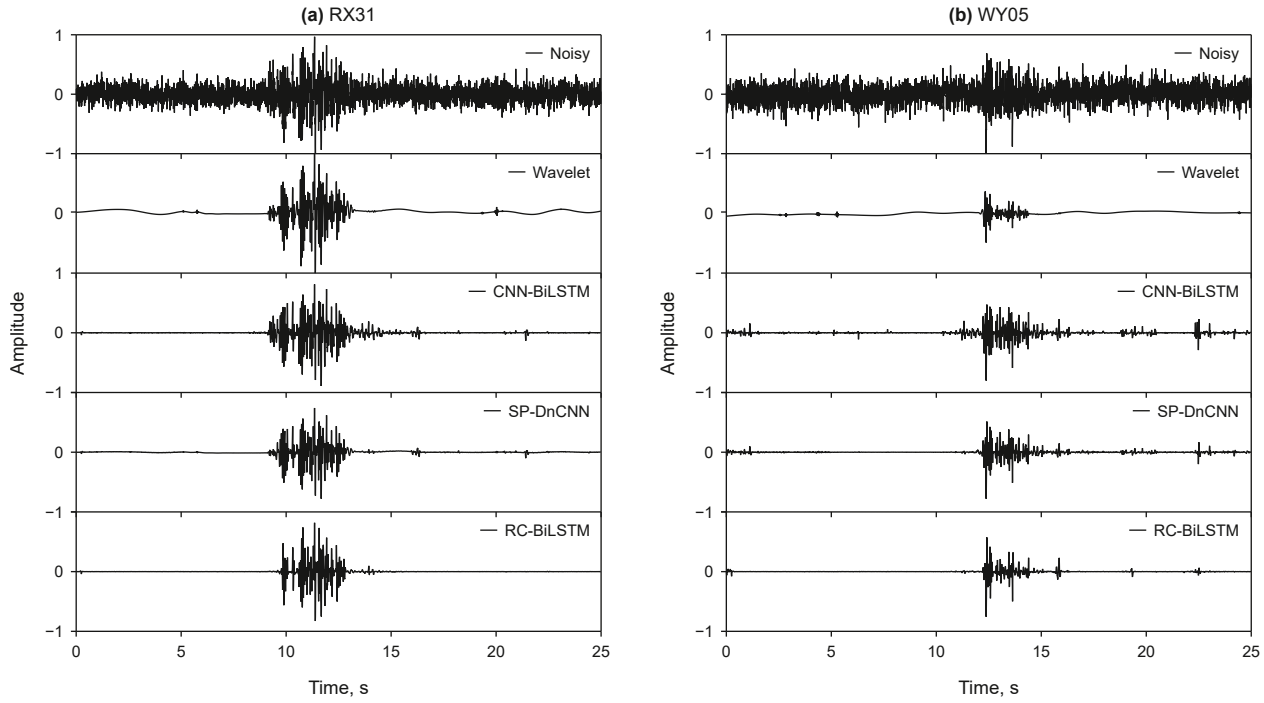


Fig. 8. Comparison of denoised waveforms obtained via different methods.

original records are strongly masked by background noise. Wavelet-based denoising attenuated part of the noise, but also introduced strong low-frequency smoothing and caused some waveform distortion. CNN-BiLSTM and SP-DnCNN recovered the main phase structure reasonably well, although local residual noise or loss of detail could still be observed. By contrast, RC-BiLSTM suppressed background noise more effectively while preserving the main phases and local waveform details.

Table 7 presents the corresponding quantitative comparison. Overall, RC-BiLSTM achieved the highest improvement in windowed *SNR*, outperforming all comparison methods, whereas SP-DnCNN performed comparably to CNN-BiLSTM. These results support the field applicability and effectiveness of the proposed method.

Finally, RC-BiLSTM was directly applied to all 9054 microseismic field data recorded in the Zigong-Neijiang area, and the distributions of windowed *SNR* before and after denoising were analyzed statistically (Fig. 9). Excluding a small fraction of invalid data, the *SNR* of nearly all microseismic events was significantly improved. In the original dataset, 65% of the traces exhibited an *SNR* below 10 dB, reflecting severe noise contamination and poor overall data quality. Events with moderate *SNRs* (10–30 dB) accounted for 34% of the total, whereas only 1% of the data possessed an *SNR* exceeding 30 dB. Conversely, the application of the proposed RC-BiLSTM model yielded a profound shift in the *SNR* distribution. The fraction of severely contaminated data (*SNR* < 10 dB) dropped to 29%. Meanwhile, signals in the 10–30 dB range increased to 50%, and high-fidelity data exceeding 30 dB reached 20%. These results indicate that RC-BiLSTM improves the windowed *SNR* distribution for the analyzed Zigong-Neijiang dataset, suggesting its potential usefulness for regional scale field data enhancement within the study area.

Table 7
Quantitative comparison of the different methods.

Observed signal	*SNR*, dB				
	Original signal	Wavelet	CNN-BiLSTM	SP-DnCNN	RC-BiLSTM
RX31	−2.5	5.4	8.8	7.8	10.7
WY05	9.2	13.8	16.2	17.6	19.5

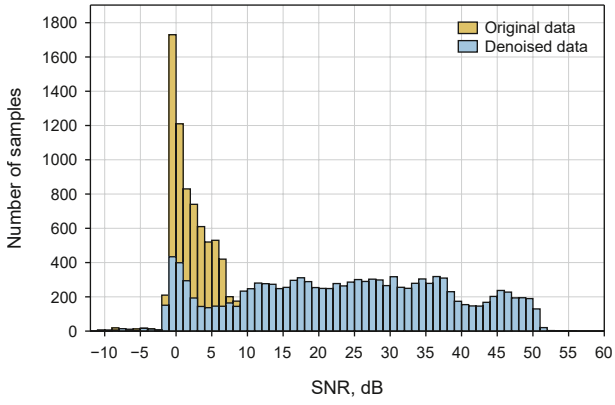


Fig. 9. Histogram of the windowed *SNR* distribution of all field data in the study region before and after RC-BiLSTM denoising.

3.2.2. Tulsa area

To further examine the applicability of the proposed method under different regional noise environments and medium conditions, the trained RC-BiLSTM model was applied to microseismic field data from the Tulsa area. The raw Tulsa records were processed using the same workflow as the Zigong–Neijiang field records, no additional Tulsa-specific preprocessing was introduced. The Tulsa records were not used for retraining, validation, or hyperparameter tuning; the trained RC-BiLSTM model was directly applied to the processed Tulsa records. The same

preprocessing procedure was also applied to the input data of all comparison methods. Fig. 10 presents the waveform comparisons after processing by different methods on Tulsa microseismic field data, and Table 8 shows the corresponding quantitative comparison.

The representative results in Fig. 10 and Table 8 show that RC-BiLSTM also improves waveform quality for Tulsa field records, although the geological setting, acquisition conditions, and noise characteristics of the Tulsa area differ from those of the study area. These representative examples suggest that the trained model retains a certain denoising capability when applied to field records from an independent area.

To further assess whether this improvement is limited to selected examples, the trained RC-BiLSTM model was applied to all 3000 microseismic field data recorded from the Tulsa area. The $\overline{SNR}$ improvement over the original data was approximately 18 dB after denoising. This full-dataset result provides more systematic evidence that the proposed framework can improve waveform quality under the tested cross-area Tulsa conditions. Nevertheless, because the Tulsa dataset represents only one external field area and strictly noise-free reference signals are unavailable for field records, these results should be interpreted as preliminary evidence of cross-area transferability rather than definitive proof of broad generalization. Broader validation using additional field datasets from different geological settings, acquisition systems, and noise environments is still required.

Table 8
Quantitative comparison of the different methods for field data.

Observed signal	*SNR*, dB				
	Original signal	Wavelet	CNN-BiLSTM	SP-DnCNN	RC-BiLSTM
16A-27	1.8	7.3	17.4	15.2	26.6
62-27	5.1	15.1	21.3	19.3	31.6

4. Discussion

First, it should be emphasized that the proposed RC-BiLSTM framework is not a strictly physics-constrained method. The stochastic dynamical-system formulation used in this study serves as a conceptual interpretation and a soft prior for the denoising process, rather than as an explicit governing-equation constraint. This design keeps the framework lightweight and reduces training cost, but it also means that the present method does not guarantee strict physical consistency. Future work will therefore explore the incorporation of stronger physics-based constraints while preserving the lightweight nature of the present framework. Possible directions include low-cost wave-propagation consistency losses or weak wave-equation residuals applied to selected stages.

Second, the present framework does not completely eliminate dependence on prior models, because the training labels are still generated from reflectivity-based forward modeling. To further mitigate the framework's reliance on synthetic training data, we have preliminarily explored transitioning the current supervised BiLSTM refinement stage into a self-supervised mode using a Noise-to-Noise (N2N) strategy. Specifically, this strategy utilizes independent noisy realizations of the same signal as training pairs, leveraging the statistical principle that the network can recover the underlying clean representation without requiring noise-free ground truth. However, the current outcomes under this self-supervised paradigm remain suboptimal, particularly in balancing the recovery of weak phases and the suppression of complex nonstationary noise. This suggests that simply integrating an N2N scheme into the residual refinement stage is insufficient for the current task. Developing more sophisticated self-supervised or weakly supervised refinement strategies therefore remains a critical direction for future work.

Third, the limitations related to training-data dependence and denoising fidelity should be explicitly acknowledged. Although field-noise segments are used to construct the noisy inputs, the

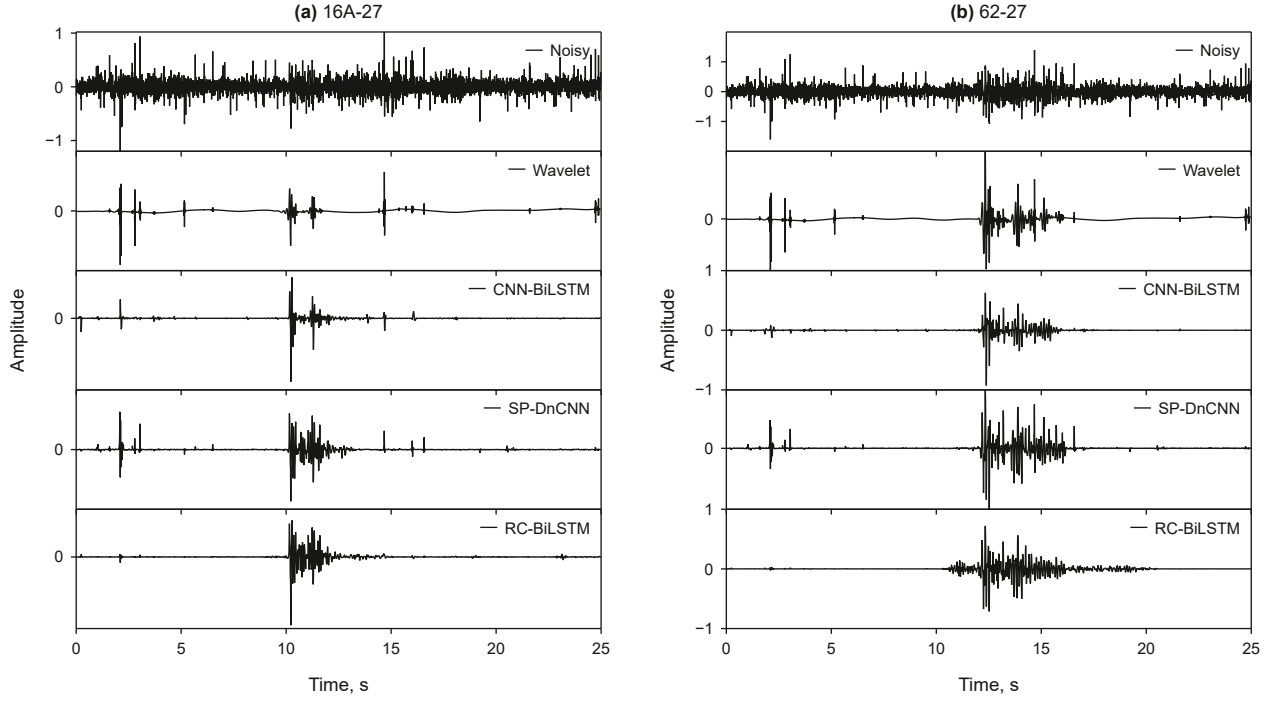


Fig. 10. Comparison of denoised waveforms obtained via different methods.

clean labels are still generated by reflectivity-based forward modeling. Therefore, the supervised BiLSTM refinement stage remains dependent on synthetic labels and on assumptions regarding the velocity structure, source mechanisms, propagation effects, and simplified recording conditions. When real field data deviate from these assumptions, data-distribution mismatch may arise in waveform characteristics, spectral content, noise type, station conditions, and source–receiver geometry, which may reduce the stability of the denoising results. Moreover, potential risks of weak-event distortion and artificial event generation should be considered. In very low-SNR cases, the network may over-smooth weak phases, attenuate small-amplitude events, or introduce arrival-time and amplitude distortions. Conversely, under strongly nonstationary or out-of-distribution noise conditions, coherent noise fragments may be enhanced into phase-like waveforms, producing artificial event-like features after denoising. Therefore, the denoised outputs should not be interpreted independently of the original records, and their reliability should be further assessed using downstream tasks such as phase picking, event detection, event localization, polarity analysis, and focal mechanism inversion. Future work will explore self-supervised or weakly supervised learning, uncertainty estimation, and lightweight physics-aware constraints to reduce synthetic-label dependence and better preserve weak-event fidelity.

5. Conclusions

This study proposes a lightweight two-stage microseismic denoising framework, RC-BiLSTM, based on a dynamical-system consistency prior. The framework combines a dynamical backbone with residual refinement, thereby improving the interpretability of the denoising process and maintaining effective denoising performance.

Numerical experiments on synthetic data demonstrate that, compared with methods such as wavelet-based denoising, CNN-BiLSTM, and SP-DnCNN, the RC-BiLSTM framework achieves superior performance in waveform recovery, spectral consistency, and quantitative evaluation metrics. Moreover, since the RC component trains only a linear readout layer, the proposed method substantially reduces training cost while maintaining good denoising performance, offering a distinct lightweight advantage. The robustness test involving medium-parameter perturbations confirms that the dynamical-system consistency prior effectively enhances the resilience to uncertainties in prior model accuracy. The field data results further confirm that RC-BiLSTM can improve the quality of microseismic field data under complex noise conditions and has practical potential for microseismic monitoring.

Overall, the present study suggests that coupling dynamical guidance with staged neural refinement is a promising direction for microseismic denoising. Future work will further reduce dependence on prior models, improve the recovery of weak phases in complex nonstationary noise environments, and explore stronger physics-based constraints while preserving the lightweight advantage of the proposed framework.

CRediT authorship contribution statement

Yi-Fei Bao: Writing – review & editing, Writing – original draft, Visualization, Validation, Supervision, Software, Resources, Project administration, Methodology, Investigation, Funding acquisition, Formal analysis, Data curation, Conceptualization. **Jian Gao:** Validation, Project administration, Methodology. **Zi-Xiang Yan:** Visualization, Investigation. **Jing-Hua Xiao:** Validation, Supervision, Project administration.

Declaration of competing interest

The authors declare that they have no known competing financial interests or personal relationships that could have appeared to influence the work reported in this paper.

Acknowledgements

This work was supported by National Natural Science Foundation of China (Grant No. 42304110).

References

Anikiev, D., Birnie, C., bin Waheed, U., et al., 2023. Machine learning in microseismic monitoring. Earth Sci. Rev. 239, 104371. https://doi.org/10.1016/j.earscirev.2023.104371.

Anvari, R., Mohammadi, M., Kahoo, A.R., 2018. Enhancing 3-D seismic data using the t-SVD and optimal shrinkage of singular value. IEEE J. Sel. Top. Appl. Earth Obs. Remote Sens. 12 (1), 382–388. https://doi.org/10.1109/JSTARS.2018.2883404.

Brandolin, F., Ravasi, M., Alkhalifah, T., 2024. PINNslope: seismic data interpolation and local slope estimation with physics-informed neural networks. Geophysics 89, 331–345. https://doi.org/10.1190/geo2023-0323.1.

Chen, J., Chen, G., Li, J., et al., 2024. Efficient seismic data denoising via deep learning with improved MCA-SCUNet. IEEE Trans. Geosci. Rem. Sens. 62, 1–14. https://doi.org/10.1109/TGRS.2024.3355972.

Duan, L., Cai, J., Wang, L., et al., 2025. Research on seismic signal denoising model based on DnCNN network. Appl. Sci. 15 (4), 2083. https://doi.org/10.3390/app15042083.

Gauthier, D.J., Bollt, E., Griffith, A., et al., 2021. Next generation reservoir computing. Nat. Commun. 12 (1), 5564. https://doi.org/10.1038/s41467-021-25801-2.

Han, J., van der Baan, M., 2015. Microseismic and seismic denoising via ensemble empirical mode decomposition and adaptive thresholding. Geophysics 80, 69–80. https://doi.org/10.1190/geo2014-0423.1.

Huang, X., Alkhalifah, T.A., 2024. Microseismic source imaging using physics-informed neural networks with hard constraints. IEEE Trans. Geosci. Rem. Sens. 62, 1–11. https://doi.org/10.1109/TGRS.2024.3366449.

Lai, G., Jiang, C., Wang, W., et al., 2023. Spatial-temporal distribution and focal mechanisms for the shallow earthquakes in the Rongchang-Luxian region in southern Sichuan Basin, China. Seismolog. Soc. Am. 94 (4), 1860–1876. https://doi.org/10.1785/0220220339.

LeCun, Y., Bengio, Y., Hinton, G., 2015. Deep learning. Nature 521, 436–444. https://doi.org/10.1038/nature14539.

Lee, D., Shin, S.R., Yeo, E.M., et al., 2024. Denoising sparker seismic data with deep BiLSTM in fractional Fourier transform. Comput. Geosci. 184, 105519. https://doi.org/10.1016/j.cageo.2024.105519.

Li, H., Shi, J., Li, L., et al., 2022. Novel wavelet threshold denoising method to highlight the first break of noisy microseismic recordings. IEEE Trans. Geosci. Rem. Sens. 60, 1–10. https://doi.org/10.1109/TGRS.2022.3142089.

Li, J., Wu, X., Hu, Z., 2022. Deep learning for simultaneous seismic image super-resolution and denoising. IEEE Trans. Geosci. Remote Sens. 60, 1–11. https://doi.org/10.1109/TGRS.2021.3057857.

Lin, J., Zheng, J., Li, D., et al., 2023. Research on microseismic denoising method based on CBDNet. Artif. Intell. Geosci. 4, 28–38. https://doi.org/10.1016/j.aiig.2023.02.002.

Meng, F., Fan, Q., Li, Y., 2022. Self-supervised learning for seismic data reconstruction and denoising. IEEE Geosci. Remote Sens. Lett. 19, 1–5. https://doi.org/10.1109/LGRS.2021.3068132.

Mousavi, S.M., Langston, C.A., 2016. Hybrid seismic denoising using higher-order statistics and improved wavelet block thresholding. Bull. Seismol. Soc. Am. 106 (4), 1380–1393. https://doi.org/10.1785/0120150345.

Mu, X., Cheng, S., Alkhalifah, T., 2025. SeparationPINN: Physics-informed neural networks for seismic P- and S-wave mode separation. IEEE Trans. Geosci. Rem. Sens. 63, 1–10. https://doi.org/10.1109/TGRS.2025.3582289.

Novoselov, A., Balazs, P., Bokelmann, G., 2022. SEDENOSS: separating and DENOising seismic signals with dual-path recurrent neural network architecture. J. Geophys. Res. Solid Earth 127 (3). https://doi.org/10.1029/2021JB023183.

Peng, P., Lei, R., Wang, J., 2023. Enhancing microseismic signal classification in metal mines using transformer-based deep learning. Sustainability 15 (20), 14959. https://doi.org/10.3390/su152014959.

Rasht-Behesht, M., Huber, C., Shukla, K., et al., 2022. Physics-informed neural networks (PINNs) for wave propagation and full waveform inversions. J. Geophys. Res. Solid Earth 127 (5). https://doi.org/10.1029/2021JB023120.

Sang, W.J., Yuan, S.Y., Yong, X.S., et al., 2021. DCNNs-based denoising with a novel data generation for multidimensional geological structures learning. IEEE Geosci. Remote Sens. Lett. 18 (10), 1861–1865. https://doi.org/10.1109/LGRS.2020.3007819.

Schimmel, M., Gallart, J., 2007. Frequency-dependent phase coherence for noise suppression in seismic array data. J. Geophys. Res. Solid Earth 112 (B4), B04303. https://doi.org/10.1029/2006JB004680.
Shao, R., Wang, H., Xiao, L., 2024. Reservoir evaluation using petrophysics informed machine learning: a case study. Artif. Intell. Geosci. 5, 100070. https://doi.org/10.1016/j.aiig.2024.100070.
Sun, F., Lin, H., Li, Y., 2025. Unsupervised seismic data denoising using diffusion denoising model. IEEE Trans. Geosci. Rem. Sens. 63, 1–14. https://doi.org/10.1109/TGRS.2025.3539279.
Wang, C., Zong, Z., Yin, X., et al., 2024. Seismic resolution enhancement with variational modal-based fast-matching pursuit decomposition. Interpretation 12, 77–86. https://doi.org/10.1190/INT-2023-0002.1.
Wang, J., Yan, Z., Gui, L., et al., 2022. Reconstruction of nonlinear flows from noisy time series. Nonlinear Dyn. 108 (4), 3887–3902. https://doi.org/10.1007/s11071-022-07388-5.
Warpinski, N., 2009. Microseismic monitoring: inside and out. J. Petrol. Technol. 61 (11), 80–85. https://doi.org/10.2118/118537-JPT.
Xie, P., Liu, Y., Liu, C., et al., 2025. Simultaneous suppression of seismic random and erratic noise using PINN with high-frequency preservation. J. Geophys. Eng. 22 (6), 1796–1808. https://doi.org/10.1093/jge/gxaf109.
Yuan, S.Y., Xu, Y.W., Xie, R.J., et al., 2025. Multi-scale intelligent fusion and dynamic validation for high-resolution seismic data processing in drilling. Petrol. Explor. Dev. 52 (3), 607–617. https://doi.org/10.1016/S1876-3804(25)60596-9.
Yao, G., Wu, D., Wang, S.X., 2020. A review on reflection-waveform inversion. Pet. Sci. 17, 334–351. https://doi.org/10.1007/s12182-020-00431-3.
Zhang, F., 2021. Simultaneous inversion for S-wave velocity and density from the SV-SV wave. Geophysics 86 (2), 187–195. https://doi.org/10.1190/geo2020-0112.1.
Zhang, H., Yang, X., Ma, J., 2020. Can learning from natural image denoising be used for seismic data interpolation? Geophysics 85 (4), 115–136. https://doi.org/10.1190/geo2019-0243.1.
Zhang, Z., Qin, G., Liang, Y., et al., 2025. Ground-truth-free 3D seismic denoising based on diffusion models: achieving effective constraints through embedded self-supervised noise modeling. Remote Sens. 17 (6), 1061. https://doi.org/10.3390/rs17061061.
Zhao, Z., Rao, Y., 2024. Seismic random noise suppression based on SP-DnCNN neural network. Chin. J. Geophys. 67 (10), 3841–3850. https://doi.org/10.6038/cjg2023R0483 (in Chinese).
Zhu, W., Mousavi, S.M., Beroza, G.C., 2019. Seismic signal denoising and decomposition using deep neural networks. IEEE Trans. Geosci. Rem. Sens. 57, 9476–9488. https://doi.org/10.1109/TGRS.2019.2926772.